SYNTHESIS, CHARACTERIZATION, AND ELECTRICAL PROPERTIES OF $([SnSe]_{1+\delta})_m(NbSe_2)_3$ FERECRYSTALLINE COMPOUNDS

by

PHUONG KIM TA

A THESIS

Presented to the Department of Chemistry and Biochemistry
and the Robert D. Clark Honors College
in partial fulfillment of the requirements for the degree of
Bachelor of Science

June, 2015

An Abstract of the Thesis of

Phuong Kim Ta for the degree of Bachelor of Science

in the Department of Chemistry and Biochemistry to be taken June, 2015

Title: Synthesis, Characterization, and Electrical Properties

of $([SnSe]_{1+\delta})_m(NbSe_2)_3$ Ferecrystalline Compounds

Approved: 

Dr. David C. Johnson

Ferecrystalline compounds $([SnSe]_{1+\delta})_m(NbSe_2)_3$, or $(m,3)$, with $1 \leq m \leq 30$ were prepared using the modulated elemental reactants (MER) technique in a vacuum deposition chamber. A 5.78(4) Å change in *c*-lattice parameter change was observed as the compounds were systematically built up in thickness, ranging from 1 to 30 layers of *m*. The *c*-lattice constants for both SnSe and $NbSe_2$ constituents found in the $(m,3)$ compound were consistent with those of the previously studied $(m,1)$ and $(m,2)$ compounds. In-plane diffraction data revealed distortion of the basal plane as the thickness of the SnSe layer increased, similar to those of the $(m,1)$ and $(m,2)$. HAADF-STEM images showed turbostratic disorder, which is the signature feature of

ferecrystals, and different polytypes of the $NbSe_2$ subunits. Metallic behavior was observed in electrical resistivity. The slight upturn in the resistivity at low temperature in higher *m* value indicates carrier localization. Carrier concentration decreases as the number of SnSe layer increases, but it decreases faster than expected, suggesting charge is transferred from the SnSe constituent to the $NbSe_2$ subunit. A change from a negative to positive slope as a function of temperature was observed in carrier mobility as *m* increases. When plotted as a function of *m/n* ratio, electrical resistivity of the (*m*,3) compounds deviates from the predicted parallel resistor model, indicating the middle $NbSe_2$ layer has a limited influence on resistivity of the compounds.

Acknowledgements

First and foremost, I would like to thank my primary thesis advisor Dr. David C. Johnson for giving me an opportunity to work in his lab and helping me throughout my undergraduate career. I would also like to thank all members in the Johnson lab and CAMCOR staff for their help and support. I would like to thank Dr. Kelly Sutherland and Miriam Jordan for their help and advice throughout the thesis process. I would like to thank our post-doc Matthias Falmbigl for all his help analyzing samples. Especially, I would like to express my sincerest gratitude towards my lab mentor, Matti Alemayehu, who guides, helps removing barriers, and encourages me to excel. Lastly, I would like to thank my family for their support and faith in my successful completion of college.

Table of Contents

INTRODUCTION 1

EXPERIMENTAL 5

RESULTS AND DISCUSSION 8

Synthesis and Characterization 8

Electrical Properties 13

CONCLUSION 18

REFERENCES 20

List of Figures

Figure 1: A schematic representation of a misfit layer compound (a), and a ferecrystal that exhibits turbostratic (rotational) disorder along the c-axis (b). 3

Figure 2: Amorphous precursors of Nb|2Se and Sn|Se forms the targeted superlattice upon annealing at the optimal condition, yielding the desired (1,3) compound. 3

Figure 3: The $([SnSe]_{1+\delta})_m(NbSe_2)_3$ compounds are expected to follow the resistors in PRM since there exists one middle layer of $NbSe_2$ that does not have any interaction with the rock salt (SnSe) layers. 5

Figure 4: Annealing study of (3,3) compound at temperatures ranging from 100 °C to 600 °C for 20 minutes (a), and a detailed view of the (00 12) reflection to emphasize the optimal annealing condition based on the narrowest line width (b). 9

Figure 5: 00*l* XRD patterns of $([SnSe]_{1+\delta})_m(NbSe_2)_3$ compounds with selected Bragg reflections indexed to the left of the corresponding peak. 10

Figure 6: In-plane diffraction pattern of the (6,3) compound. The inset shows the *hk*0 XRD patterns of selected compounds in the (m,3) series. (*) marks in the inset indicate substrate peaks. 11

Figure 7: HAADF-STEM images of the (5,3) compound, showing consistent layering of constituents in (a), (110) orientation of SnSe layers in (b), and two different polytypes of $NbSe_2$ layers in (c). 12

Figure 8: Metallic behavior seen in temperature-dependent resistivity for all compounds. 13

Figure 9: Carrier concentration is plotted as a function of temperature. 15

Figure 10: The double logarithmic carrier mobility plotted as a function of temperature. 16

Figure 11: Plots of resistivity at room temperature (a) and carrier density at room temperature as a function of m/n ratio (b). All dashed black lines are used only to guide the eye. 17

Figure 12: Carrier mobility at room temperature is plotted against *m/n* ratio. All dashed black lines are used only to guide the eye. 18

List of Tables

Table 1: *c*-lattice parameters of the $([SnSe]_{1+\delta})_m(NbSe_2)_3$ compounds as a function of *m* 9

Table 2: In-plane lattice parameters of the $([SnSe]_{1+\delta})_m(NbSe_2)_3$ compounds as a function of *m*..... 10

INTRODUCTION

Due to the fast development in the semiconductor industry, a greater motivation to more comprehensive and in-depth research that focuses on the elemental and structural studies of nanostructured compounds continues to be an immense field of curiosity and mysteries for exploration.[1] Devices are getting smaller but more functional day by day; hence, the ability to pack more functions per unit area is crucial to maximize efficiency in nanodevices.[2] Since both structural and chemical components that make up nanomaterials are closely associated with their electrical and thermal properties, not only is it important to understand the synthesis technique, but it is also crucial to develop processing methods that will yield better quality materials.

Nanomaterials lie at the intersection of chemistry, physics, materials science, and biology, and pose many latent and promising applications in the future. Potential opportunities and applications include but are not limited to development and advancement of low power, high frequency, and flexible electronic nanodevices.[3] Due to their ability to be easily incorporated into devices, transitional metal dichalcogenides have recently been a focus of study. Transitional metal dichalcodgenides are trilayer X-T-X sandwiches where X = S or Se and T = a transitional metal. A single layer of $MoSe_2$ has successfully been used to manufacture phototransistors, low-power field effect transistors, and logic circuits.[4–6] Nanostructured compounds of niobium dichalcogenides (NbX_2 where X = S or Se) may be used for applications such as optical antenna, ultrasensitive surface-enhanced optical bio-sensing, and quantum processing.[7–

[9] $NbSe_2$ has been extensively studied for the past few decades[10–12] because it possesses two unusual electrical transport properties: superconductivity and charge density waves.

There exist a large number of undiscovered compounds based on these 2D materials. A number of 3D comprehensive inorganic compounds composed of 2D interwoven constituents with distinctive structures and properties are shaping the face of the new era of materials research.[13] Misfit layer compounds (MLCs) and ferecrystals (FCs) are examples of these 2D interwoven materials. These compounds consist of a slab of a TX_2 dichalcogenide layer interwoven with a slab of a rock salt MX structure, and they exhibit the general formula of $([MX]_{1+\delta})_m(TX_2)_n$, where *m* represents the repeating units of the rock salt layer, and *n* refers to the repeating units of the dichalcogenide layer.[12] The inability to access the kinetic products of a given misfit layer compound has limited the study of misfit layer compounds to *m* values of 1 and *n* value of 1-3. In traditional misfit layer compounds, only thermodynamic products can be accessed due to the high diffusion length and the high temperature synthesis method that is required to initiate nucleation.

In contrast to misfit layer compounds, ferecrystals can be synthesized at lower temperatures by reducing the diffusion length between reactants to trap kinetically stable compounds. The term ferecrystals (FCs), derived from the Latin root "*fere*-", gives the meaning of almost crystals.[14] A turbostratic (rotational) disorder between subsequent subunits of the ferecrystalline compounds exist. These compounds exhibit long-range order in the *a*-*b* plane and short-range order in the *c*-axis. Figure 1 shows a schematic representation of the difference between misfit layer compounds and ferecrystals.

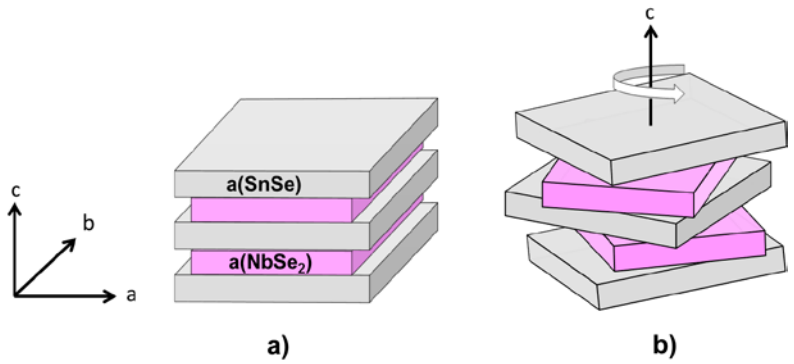

Figure 1: A schematic representation of a misfit layer compound (a), and a ferecrystal that exhibits turbostratic (rotational) disorder along the c-axis (b).

The research reported here focuses on the structure-property relationship of intergrowth compounds $([SnSe]_{1+\delta})_m(NbSe_2)_3$, or (*m*,3). Modulated Elemental Reactant (MER) technique was used to synthesize the compounds in this study. The technique allows the precise control of thickness and composition, which leads to shorter diffusion length, which in turn allows access to kinetically stable products. These low temperature compounds are annealed under a N_2 inert atmosphere to promote self-assembly of the precursor. Figure 2 displays an atomic representation of a ferecrystal with three dichalcogenide layers of $NbSe_2$ and one layer of a rock salt unit: SnSe.

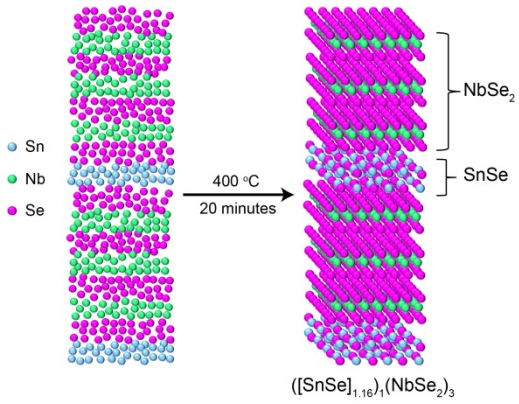

Figure 2: Amorphous precursors of Nb|2Se and Sn|Se forms the targeted superlattice upon annealing at the optimal condition, yielding the desired (1,3) compound.

This study also continues the work of Alemayehu *et al*[15,16] to explore the extent of charge transfer and electrical properties of the (*m*,3) compounds in comparison to the previously reported series of ferecrystals: $([SnSe]_{1.16})_m(NbSe_2)_1$, or (*m*,1)[15] and $([SnSe]_{1.16})_m(NbSe_2)_2$, or (*m*,2)[16]. It is hypothesized that the (*m*,3) compounds will obey the parallel resistor model (PRM) because there is one pristine layer of $NbSe_2$ that does not interact with the insulating layer. Tin selenide (SnSe) has the capacity to donate charge and is an *n*-type semiconductor depending on the doping level: conducts through heavy electrons.[17] In contrast, niobium diselenide ($NbSe_2$) has the ability to accept or donate charge and is a *p*-type conductor: conducts through empty states.[18–20] Previously, compounds that belong to the (*m*,1) and $([PbSe]_{1.14})_m(NbSe_2)_1$ families were both synthesized and thoroughly studied by Alemayehu *et al*,[15,21] who introduced the PRM to explain the resistivity of a single $NbSe_2$ layer. The PRM treated the $NbSe_2$ layer as the only conducting constituent and the PbSe as the insulating constituent. The resistivity of the single $NbSe_2$ layer in each compound could be extracted using Equation 1.[21]

$$\rho_{NbSe_2} = \rho_{eff}\left(\frac{n}{m+n}\right) \quad (1)$$

where ρ_{NbSe_2} is the resistivity of the $NbSe_2$ layer, ρ_{eff} is the total resistivity of the compound, *m* is the number of rock salt layers, and *n* is the number of $NbSe_2$ layers. Based on the assumption that there is no interlayer interaction between the subunits, the model is used to predict the resistivity of the single conducting layer, $NbSe_2$. Recently, a series of compounds in the (*m*,1) and (*m*,2) families were prepared. The parallel resistors model was then applied to (*m*,1) compounds, but similar to the analogous $([PbSe]_{1.14})_m(NbSe_2)_1$ compounds, interlayer interaction between the insulating layer

and the conducting layer was observed. In the (*m*,2) compounds, where there were two $NbSe_2$ layers interfacing with SnSe, similar observations with the single layer $NbSe_2$ series were made. The electrical properties of both (*m*,1) and (*m*,2) compounds deviated from the parallel resistor model, indicating the presence of interlayer interaction between the subunits. If the number of $NbSe_2$ layer is increased to three as in the (*m*,3) compounds where $1 \leq m \leq 30$, these series of compounds might obey the PRM, since one layer of $NbSe_2$ will be "sandwiched" in between two other $NbSe_2$ layers and will have no direct interaction with the insulating constituent (SnSe) as seen in Figure 3.

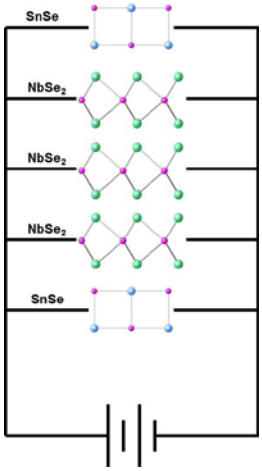

Figure 3: The $([SnSe]_{1+\delta})_m(NbSe_2)_3$ compounds are expected to follow the resistors in PRM since there exists one middle layer of $NbSe_2$ that does not have any interaction with the rock salt (SnSe) layers.

EXPERIMENTAL

$([SnSe]_{1+\delta})_m(NbSe_2)_3$ with $1 \leq m \leq 30$ precursor compounds were synthesized using the Modulated Elemental Reactant (MER) technique in a custom-built vapor deposition chamber at base pressure of 1×10^{-7} Torr. Elemental sources of Sn (99.98% purity) and Nb (99.9% purity) were evaporated using 3kW Thermionics electron beam guns at rates of 0.02 nm/sec and 0.04 nm/sec respectively. Selenium (99.995% purity)

was evaporated from an effusion cell at a deposition rate of 0.05%. Quartz crystal monitors were placed 25 cm above each source to control the deposition rates. The substrates were mounted on a computer-controlled motorized stage. A custom-made LabVIEW program rotated the sample into position above deposition sources, and sequentially opened and closed the shutters following the preprogramed times and thicknesses. This process was repeated, building up the precursor layer-by-layer until the sample was about 400 to 600 Å thick. Desired precursors were deposited onto silicon wafer substrates, which were used for X-ray measurements, and quartz substrates, which were used for electrical measurements, after annealing.

Prior to X-ray and electrical measurements, the amorphous precursors were analyzed by X-ray reflectivity (XRR) and were annealed in a N_2 inert atmosphere (≤ 0.7 ppm O_2) at 400 °C for 20 minutes. Annealing parameters were optimized based on ideal diffraction patterns. Both high and low angles X-ray analyses were performed on Bruker AXS D8 diffractometer equipped with a Cu Kα (1.54 Å) radiation source, a Gobel mirror, and Bragg-Brentano optics geometry operated at 40 kV and 40 mA. Low angle (0-6° 2θ) and high angle (3-65° 2θ) diffraction scans were obtained using locked coupled θ-2θ geometry to determine the total thickness and repeat thickness of the compounds. Calculations of total film thickness using XRR patterns and *c*-lattice parameter after annealing were discussed in detail previously in the literature.[22,23] In-plane X-ray diffraction data was carried out using the Rigaku SmartLab X-ray Diffractometer (1.54 Å) to determine the *ab*-plane lattice parameters.

Electrical resistivity and Hall effects were measured using the van der Pauw technique, using indium to create contacts between the Cu wires and the film.[24]

Electrical resistivity was measured as a function of temperature, ranging between 11 K and 295 K. Hall effect measurements were carried out at a constant current of 0.100 A with magnetic fields of 0-1.6 T. A Keithley 2181A nanovoltmeter was used to measure the potential difference between two arms of the cross as the potential difference was induced to pass through the other two arms. After determining the slope of the current-voltage curve, sheet resistance was calculated. Total thickness of the film was used to find the total resistivity of the compound.[25]

Electron Probe Micro-Analysis (EPMA) performed on a Cameca SX-100 was used to determine the composition ratios between elements through a thin-layer technique described by Phung *et al*.[26] Pieces of precursors and annealed film on Si substrates were glued onto Al pugs for measurement. Standards of Sn, Nb, Se, Si, and MgO were used as references to quantify the atomic composition of the analyzed samples. Accelerated voltages of 10, 12, and 15 keV were used to collect intensities through a thin-layer technique previously described by Donovan *et al*.[27] Composition of compounds was calculated from the acquired signal from the film and substrate as a function of accelerating voltage.[28]

Scanning Transmission Electron Microscopy (STEM) samples were prepared by film thinning and cleaning using an FEI NOVA Nanolab Dual Beam FIB equipped with side winder ion column and performed on the FEI Titan 80-300. TEM/STEM equipped with a high angle annular dark field (HAADF) described by Nellist and Nellist *et al*[29,30] was used to obtained STEM images.

RESULTS AND DISCUSSION

Synthesis and Characterization

A detailed discussion of the synthesis process to form the desired ferecrystalline compounds from modulated precursors is emphasized elsewhere by Alemayehu and coworkers.[25] Concisely, the synthesis of (*m*,3) series requires calibrating its precursor for correct thickness and stoichiometry that will yield one unit cell of the $([SnSe]_{1+\delta})_m(NbSe_2)_3$ compound. Synthesizing (*m*,3) compounds requires depositing *m* layers of SnSe and 3 layers of $NbSe_2$. Each bilayer of SnSe and trilayer of $NbSe_2$ requires composition ratios of 1:1 and 2:1 for Se/Sn and Se/Nb respectively along with stoichiometric ratio of Sn/Nb targeted at 1.16:1. Excess amount of Se (~ 4-5%) is deposited to compensate for the loss of selenium through vaporization during annealing. In order to find the optimal conditions for the compounds to self-assemble, six equal pieces of the same (3,3) compound were annealed at temperatures ranging between 100 °C to 600 °C for 20 minutes as shown in Figures 4a) and 4b). The XRD pattern after annealing at 400 °C for 20 minutes shows the narrowest full width at half maximum (FWHM) as well as the highest intensity for the 00*l* reflections, highlighting that this is the optimal annealing condition. The 00*l* scans at 500 °C and 600 °C for 20 minutes display a significant decrease in intensity as seen in Figure 4a, indicating the decomposition of the compound. All samples of the (*m*,3) family reported in this study are annealed at 400 °C for 20 minutes.

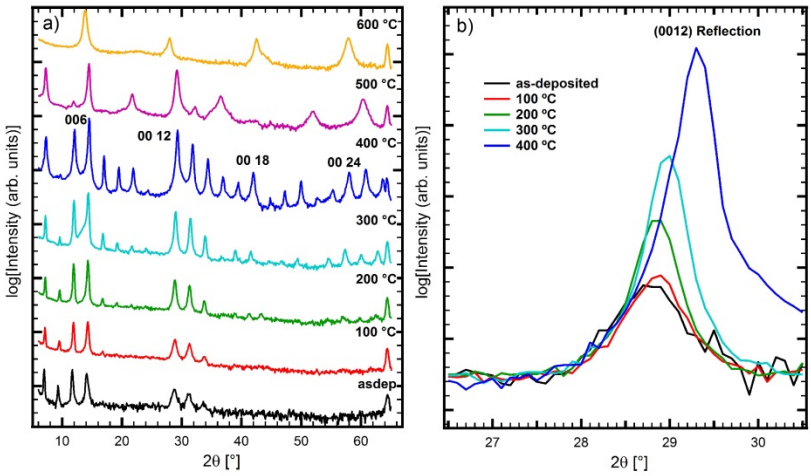

Figure 4: Annealing study of (3,3) compound at temperatures ranging from 100 °C to 600 °C for 20 minutes (a), and a detailed view of the (00 12) reflection to emphasize the optimal annealing condition based on the narrowest line width (b).

Diffraction patterns of (*m*,3) ferecrystals are displayed in Figure 5 with 00*l* Bragg reflections from the repeating units of the respective compounds, showing that the film is crystallographically aligned to the substrate. The *c*-lattice parameters of the compounds increase dependently as a function of SnSe layers (*m*) thickness increases as presented in Table 1.

Table 1: *c*-lattice parameters of the $([SnSe]_{1+\delta})_m(NbSe_2)_3$ compounds as a function of *m*

m [number of SnSe layers]	*c*-lattice parameters [Å]	FWHM [°] at 14°
1	24.92(7)	0.242
2	30.50(5)	0.285
3	36.56(6)	0.272
4	42.20(1)	0.264
5	47.97(8)	0.238
6	53.81(9)	0.243
30	192.20(5)	0.228

The *c*-lattice parameters of all compounds are plotted as the function of *m*, and the slope obtained from linear fit represents the thickness of one SnSe layer with a value of 5.78(4) Å. With error already taken into account, the calculated value from this study

is the same as the SnSe thickness found in the (*m*,1) and (*m*,2) compounds, 5.77(5) Å and 5.78(3) Å respectively, as reported by Alemayehu *et al*.[15,16]

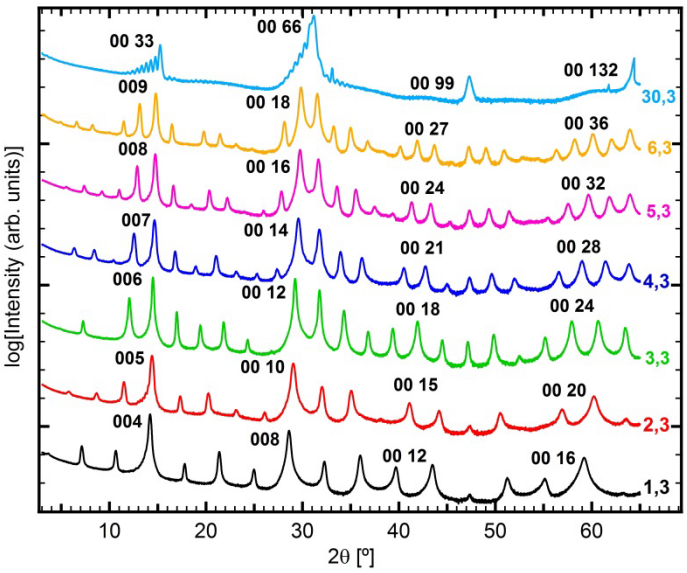

Figure 5: 00*l* XRD patterns of $([SnSe]_{1+\delta})_m(NbSe_2)_3$ compounds with selected Bragg reflections indexed to the left of the corresponding peak.

The thickness of one $NbSe_2$ layer studied here, 6.36(1) Å, is slightly smaller than the previously reported $NbSe_2$ layer in the (*m*,1) but is the same as that of the (*m*,2) compounds, whose one single dichalcogenide layer has the thicknesses of 6.48(8) Å and 6.40(5) Å, respectively. The *c*-lattice parameter of $NbSe_2$ layer falls within the reported values of 6.30 Å found in $([PbSe]_{1.14})_1(NbSe_2)_n$ to 6.38(2) Å found in $([PbSe]_{1.10})_1(NbSe_2)_n$ as described by Alemayehu *et al* and Oosawa *et al* respectively.[21,31] Kershaw *et al* also reported a thickness range of 6.28-6.35 Å for an isolated binary $NbSe_2$.[32]

Table 2: In-plane lattice parameters of the $([SnSe]_{1+\delta})_m(NbSe_2)_3$ compounds as a function of *m*

m	*a*-lattice of SnSe [Å]	*b*-lattice of SnSe [Å]	*a*-lattice of $NbSe_2$ [Å]	Misfit (δ)
1	5.98(1)	-	3.46(1)	0.16
4	4.307(1)	4.219(3)	3.47(1)	0.15
6	4.320(3)	4.221(4)	3.46(1)	0.14

The observed in-plane reflections seen via grazing incident in-plane diffraction are the result of two distinguished crystal structures of SnSe and $NbSe_2$ as observed in Figure 6 and the inset. The in-plane lattice parameters are summarized in Table 2. Similar to the work of Beekman *et al*[33] and Alemayehu *et al*[25], the reflections of SnSe can be indexed using rectangular basal plane of a 3D-orthorhombic structure whereas the Bragg peaks of $NbSe_2$ subsystem can be indexed using hexagonal basal plane.

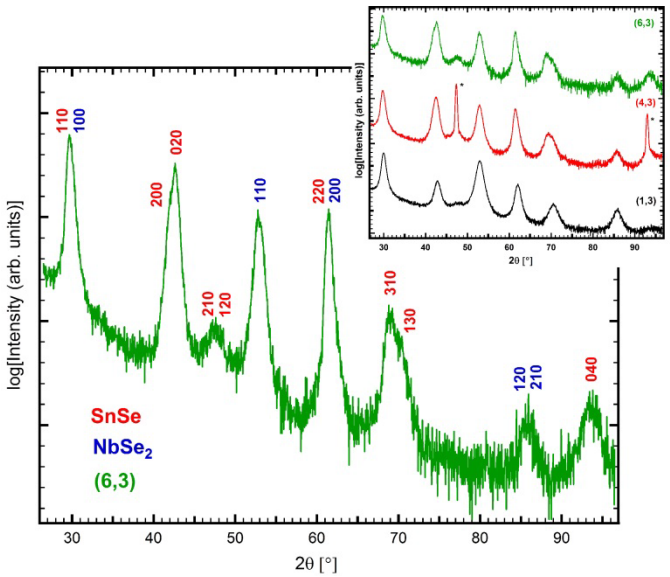

Figure 6: In-plane diffraction pattern of the (6,3) compound. The inset shows the *hk*0 XRD patterns of selected compounds in the (m,3) series. (*) marks in the inset indicate substrate peaks.

The observed *a*-lattice parameters of the $NbSe_2$ subunit, 3.46(1)-3.47(1) Å, fall within *a*-lattice parameter ranges for bulk 2*H*-$NbSe_2$ polytype (3.449-3.460 Å) but is slightly larger than bulk 4*H*-$NbSe_2$ polytype, 3.433-3.444 Å.[20,34] It is also within the range of *a*-lattice parameters observed by Wiegers *et al* for $NbSe_2$ in misfit layer compounds: 3.429-3.449 Å.[12] Similar to the (*m*,1) compounds, *a*-lattice parameters stay constant for $NbSe_2$ throughout (*m*,3) compounds. For the SnSe constituent, there is no rectangular distortion observed in the (1,3) compound, thus its *a*-lattice parameter gives

an expected value of 5.98(1) Å. Due to its basal plane distortion, which is seen clearly in compound (6,3) shown in Figure 6, the *a*-lattice parameters of the SnSe constituent in higher *m* compounds deviates from that of the (1,3) but still fall within the reported range of the (*m*,1) compounds, 4.256(4)-4.354(3) Å.[15]

Information about *b*-lattice parameter is also obtained from *hk*0 diffraction, reporting values of 4.219(3) in (4,3) and 4.221(4) Å in (6,3) compounds. Bulk SnSe as reported by Krebs has an *a*-lattice parameter of 4.441 Å and *b*-lattice constant of 4.161 Å.[35] This shows that the (*m*,3) compounds exhibits slightly smaller *a*-lattice constants and somewhat larger *b*-lattice parameters than SnSe bulk structure. Changes in in-plane lattice constants of SnSe result in a misfit parameter (δ) deviation from 0.16 in the (1,3) compound to 0.14 in the (6,3) compound. A similar observation in misfit parameters variation of $\pm$0.02 due to an increase in the area of the SnSe as a function of *m* was also previously reported by Alemayehu and coworkers.[15]

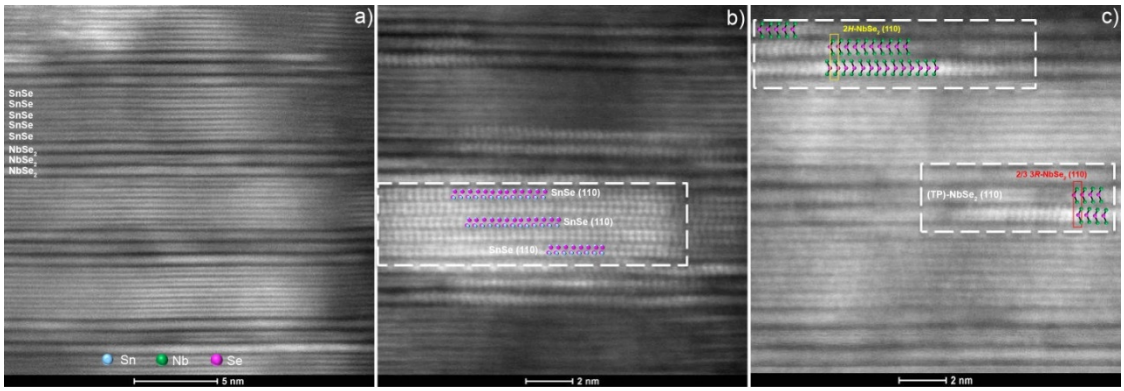

Figure 7: HAADF-STEM images of the (5,3) compound, showing consistent layering of constituents in (a), (110) orientation of SnSe layers in (b), and two different polytypes of $NbSe_2$ layers in (c).

To gain a better understanding into the structural features of these compounds, high angle annular dark field scanning transmission electron microscopy (HAADF-STEM) images were collected. HAADF-STEM images of a (5,3) compound are

displayed in Figure 7. Five consecutive double SnSe layers followed by three units of $NbSe_2$ trilayer are observed. The different orientation observed in each layer of the constituent points towards the presence of turbostratic disorder between subsequent layers, which is the signature feature of ferecrystals. In Figure 7a, the darker layer corresponds to the $NbSe_2$ subsystem while the brighter layer represents the SnSe constituent. Figure 7b shows (110) oriented SnSe while a trigonal prismatic coordination for the Nb in the $NbSe_2$ layer is highlighted in Figure 7c. Figure 7c also shows the a portion of the $NbSe_2$ layer that crystallizes as 2*H*- and 2/3rd of a 3*R*-polytype as previously reported in higher order $NbSe_2$ compounds by Alemayehu *et al.*[36]

Electrical Properties

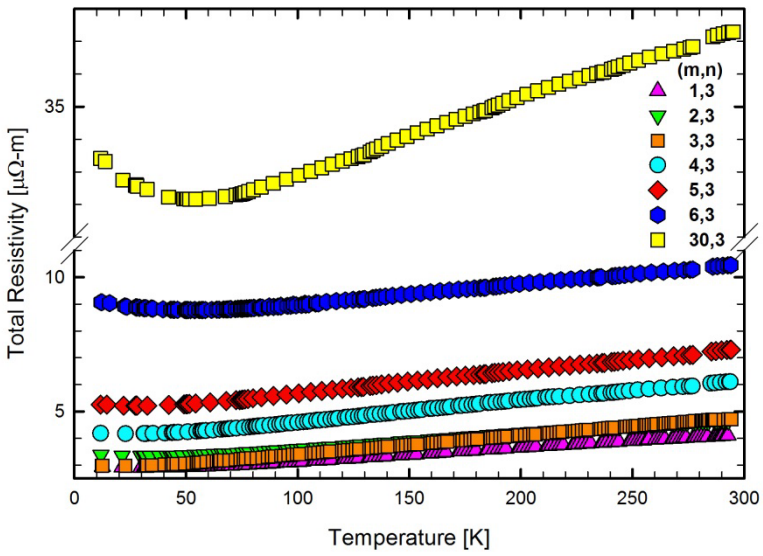

Figure 8: Metallic behavior seen in temperature-dependent resistivity for all compounds.

Previous reports on $NbSe_2$-containing misfit layer compounds and ferecrystals suggest that conduction is dominated by the $NbSe_2$ constituent,[12,15,21] so the resistivity of the $([SnSe]_{1+\delta})_m(NbSe_2)_3$ compounds expectedly increases as the number of insulating layer SnSe grows while $NbSe_2$ thickness remains constant. Figure 8 displays temperature dependent resistivity for compounds with $1 \leq m \leq 30$. Metallic temperature-dependent resistivity trend is observed for all compounds, similar to the (*m*,2) compounds and bulk-$NbSe_2$.[37] In the (*m*,1) ferecrystals, semiconductor-like behavior is seen in higher *m* values (*m* = 6-10).

In contrast, all compounds exhibit metallic behavior even at higher values of *m* in both (*m*,2) and (*m*,3) series. Like the (15,2) and (20,2) compound, the (30,3) ferecrystal also has a slight upturn at low temperature, suggesting localization of carriers. The trend in resistivity observed in Figure 8 rises surprisingly higher than the normal rate expected of linearly adding more *m* layers, and a similar observation is also seen in the (*m*,1) and (*m*,2) compounds. This occurrence is attributed to either decrease in carrier concentration and/or carrier mobility.

Bulk $NbSe_2$ was previously reported to conduct dominantly through empty states, thus it is considered to be a *p*-type conductor.[18,37] In contrast, bulk SnSe can be either *n*- or *p*-type, depending on its dopants.[17,38,39] The measured Hall coefficient values of all ferecrystals reported here are all positive, which is indicative of holes being the dominant carriers in these compounds. This observation is similar to Hall coefficients reported for $NbSe_2$ bulk material as well as the (*m*,1) and (*m*,2) compounds.

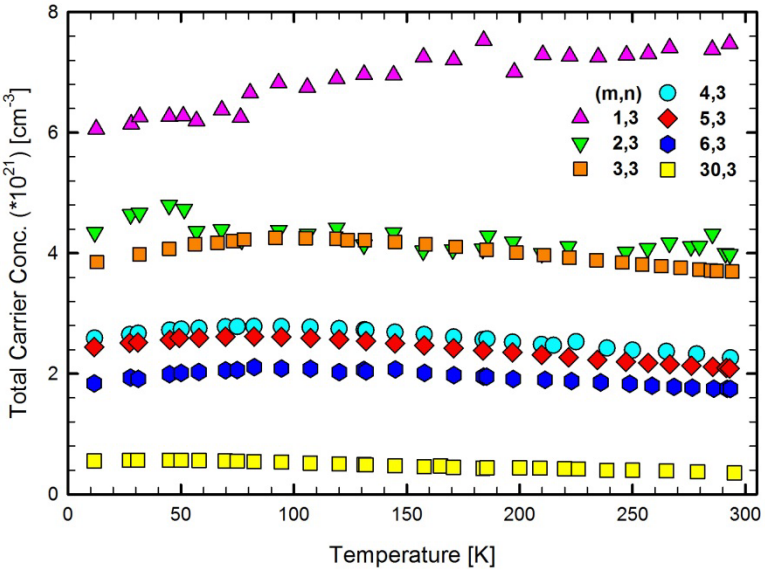

Figure 9: Carrier concentration is plotted as a function of temperature.

To better understand the trend in resistivity of the (*m*,3) compounds, temperature dependence carrier concentration is plotted in Figure 9, where carrier density is calculated from values obtained from measured Hall coefficient data, assuming a single band model. Carrier concentration of all compounds decreases as the number of SnSe increases, indicating the presence of charge transfer from the insulating layer SnSe to conducting constituent $NbSe_2$. This systematic drop in carrier concentration corresponds inversely to a steady rise in resistivity trend seen in Figure 9. Similar trends in both resistivity and carrier concentration are observed in the (*m*,1) and (*m*,2) compounds.

A log-log graph of mobility as a function of temperature is shown in Figure 10. Carrier mobility is derived from the measured resistivity and Hall coefficient data, using a single-band model approximation. As previously seen by Alemayehu and coworkers, mobility of the compounds is dominated by carriers of $NbSe_2$ at lower values of *m*, but carriers of SnSe contributes more at higher *m* values, switching the temperature dependence of the mobility in an analogous (*m*,2) series of compounds.[16] Comparable

observation is also seen in the (*m*,3) compounds reported here, where the slope of carrier mobility slowly changes from a negative to a positive at higher values of *m*.

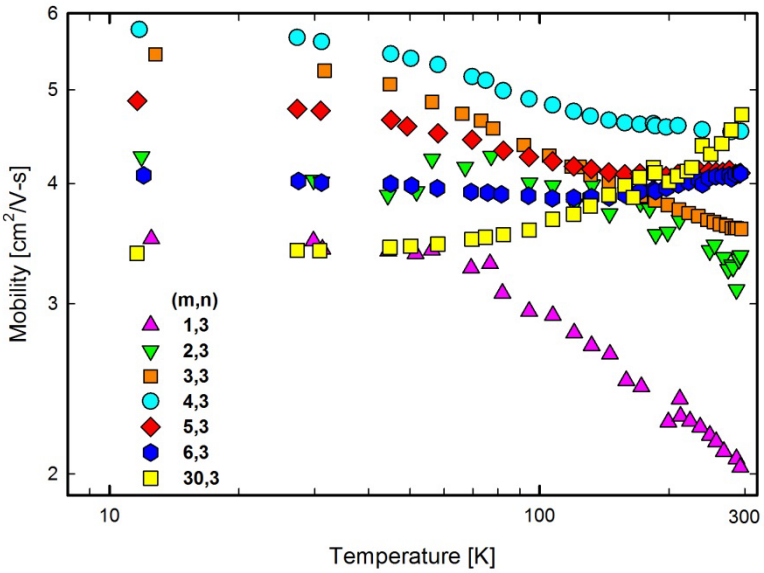

Figure 10: The double logarithmic carrier mobility plotted as a function of temperature.

Figures 11 shows electrical data of the (*m*,3) compounds at room temperature as the function of *m/n* ratio. At lower *m* values, the resistivity at room temperature for the (*m*,3) are very similar to those of the (*m*,1) and (*m*,2) compounds, indicating that adding more layers of SnSe has limited contribution to the electrical resistivity of the ferecrystals as seen in Figure 11a. The red dashed line shows the predicted resistivity of the (1,1) compound as if the $NbSe_2$ constituent had no interactions with the SnSe insulating subunit. One would expect the resistivity of the (*m*,3) compounds to fall on the predicted line and follow the PRM, for it consists of a $NbSe_2$ middle layer that does not interface with the SnSe layer. However, similar to the (*m*,1) and (*m*,2) compounds, the resistivity at room temperature of the (*m*,3) deviates from the predicted model, suggesting that the middle $NbSe_2$ constituent has limited influence on the electrical

resistivity of the system despite of its “sandwiched” position within the other two layers of $NbSe_2$.

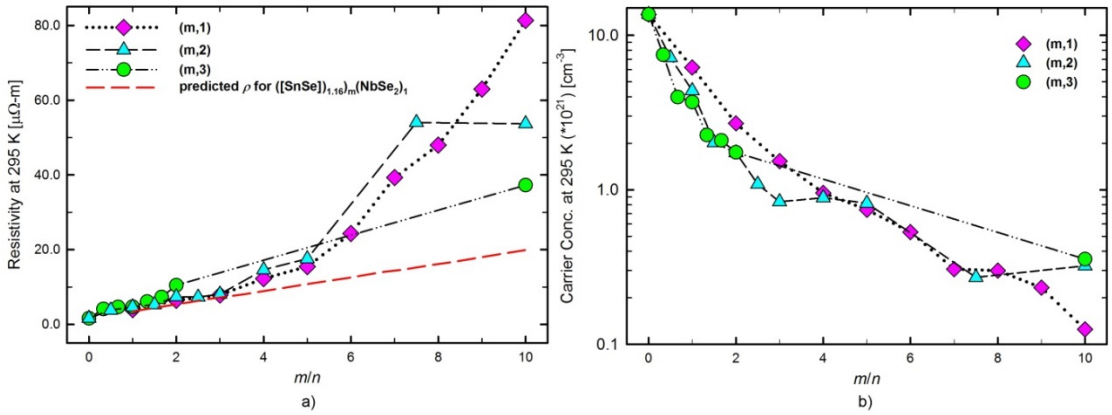

Figure 11: Plots of resistivity at room temperature (a) and carrier density at room temperature as a function of m/n ratio (b). All dashed black lines are used only to guide the eye.

Furthermore, carrier concentration values of compounds with the same *m/n* ratio in the (*m*,3) are almost the same as the (*m*,2), indicating the amount of charge transfer between the layers for the two series is relatively similar. As suggested by Alemayehu and coworkers,[16] the thickness limit of charge transfer is reached in the (20,2) compound. The (30,3) has almost the exact value of carrier concentration as the (20,2) as shown in Figure 11b.

Mobility at 295 K is plotted as a function of *m/n* ratio for the (*m*,1), (*m*,2), and (*m*,3) series as displayed in Figure 12. At lower *m/n* ratios, carrier mobility across three series of ferecrystalline compounds with the same *m/n* ratio show very slight changes in values. Furthermore, mobility data at room temperature of compounds with the lowest *m/n* ratio almost have the same value. Compounds (20,2) and (30,3) have the same carrier mobility. This once again validates that the difference in interfaces in general has

little to no effects in compound with the same *m/n* ratio as previously suggested by Alemayehu *et al.*[16]

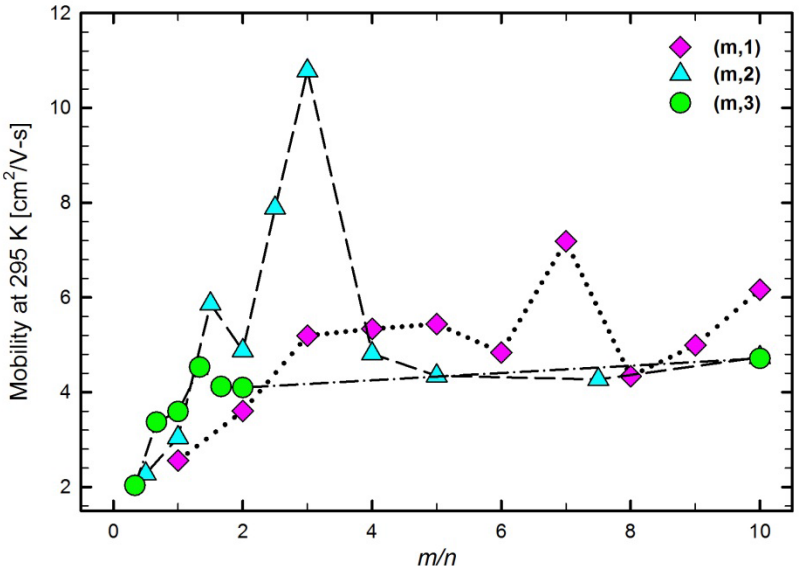

Figure 12: Carrier mobility at room temperature is plotted against *m/n* ratio. All dashed black lines are used only to guide the eye.

CONCLUSION

Structurally, the (*m*,3) compounds are similar to that of the (*m*,1) and (*m*,2). STEM images of the (5,3) compound show turbostratic disorder between subsequent layers and the presence of multiple stacking possibilities also found in (*m*,2) compounds, which can explain the lower mobility of the (*m*,3) compound in comparison to (*m*,1) and (*m*,2). In-plane diffraction shows the basal plane of the SnSe distorts as a function of SnSe thickness similar to the (*m*,1) and (*m*,2) compounds. Metallic temperature dependent resistivity was observed, which is consistent with what was observed for the (*m*,1) and (*m*,2) compounds.

Although the (m,3) compound has one single $NbSe_2$ layer which does not interface with the insulating layer SnSe, it has limited influence on the electrical resistivity of the compounds. The (*m*,3) series has relatively comparable amount of charge transfer compared to the (*m*,1) and (*m*,2) compounds.

REFERENCES

(1) Anderson, M. Novel misfit layer systems: Synthesis and characterization, University of Oregon, 2011.

(2) Moore, G. E. *Proc. IEEE* **1998**, *86*, 82–85.

(3) Wang, Z.; Su, Q.; Yin, G. Q.; Shi, J.; Deng, H.; Guan, J.; Wu, M. P.; Zhou, Y. L.; Lou, H. L.; Fu, Y. Q. *Mater. Chem. Phys.* **2014**, *147*, 1068–1073.

(4) Yin, Z.; Li, H.; Jiang, L.; Shi, Y.; Sun, Y.; Lu, G. *ACS Nano* **2011**, *6*, 74–80.

(5) Radisavljevic, B.; Radenovic, a; Brivio, J.; Giacometti, V.; Kis, a. *Nat. Nanotechnol.* **2011**, *6*, 147–150.

(6) Radisavljevic, B.; Whitwick, M.; Kis, A. *ACS Nano* **2011**, *5*, 9934–9938.

(7) Novotny, L.; van Hulst, N. *Nat. Photonics* **2011**, *5*, 83–90.

(8) Rodríguez-Lorenzo, L; Alvarez-Puebla, Ramon; Pastoriza-Santos, Isabela; Mazzucco, Stefano; Stephan, Odile; Kociak, Mathieu; Liz-Marzan, Luis; Garcia de Abajo, F. J. *J. Am. Chem. Soc.* **2009**, *131*, 4616–4618.

(9) Gonzalez-Tudela, a.; Martin-Cano, D.; Moreno, E.; Martin-Moreno, L.; Tejedor, C.; Garcia-Vidal, F. J. *Phys. Rev. Lett.* **2011**, *106*, 020501.

(10) Yoffe, J. A. W. and A. D. *Adv. Phys.* **1969**, *18*, 193–335.

(11) Mahajan, J. A. W. F. J. D. S. S. *Adv. Phys.* **1975**, *24*, 117–197.

(12) Wiegers, G. A. *Prog. Solid State Chem.* **1996**, *24*, 1–139.

(13) Beekman, M.; Heideman, C. L.; Johnson, D. C. *Semicond. Sci. Technol.* **2014**, *29*, 064012.

(14) Atkins, R.; Disch, S.; Jones, Z.; Haeusler, I.; Grosse, C.; Fischer, S. F.; Neumann, W.; Zschack, P.; Johnson, D. C. *J. Solid State Chem.* **2013**, *202*, 128–133.

(15) Alemayehu, M. B.; Falmbigl, M.; Ta, K.; Grosse, C.; Westover, R. D.; Bauers, S. R.; Fischer, S. F.; Johnson, D. C. *Chem. Mater.* **2015**, *27*, 867–875.

(16) Alemayehu, M. B.; Ta, K.; Falmbigl, M.; Johnson, D. C. *Nanoscale* **2015**, *Accepted*.

(17) Martínez-Escobar, D.; Ramachandran, M.; Sánchez-Juárez, a.; Narro Rios, J. S. *Thin Solid Films* **2013**, *535*, 390–393.

(18) Edwards, J. S. Electrical Conduction in Niobium Selenide, Simon Fraser University, 1971.

(19) Frindt, R. *Phys. Rev. Lett.* **1972**, *28*, 299–301.

(20) Meyer, S. F.; Howard, R.E.; Steward, G.R.; Acrivos, J. V.; Geballe, T. H. *J. Chem. Phys.* **1975**, *62*, 4411.

(21) Alemayehu, M. B.; Mitchson, G.; Hanken, B. E.; Asta, M.; Johnson, D. C. *Chem. Mater.* **2014**, *26*, 1859–1866.

(22) Kiessig, H. *Naturwissenschaften* **1930**, *18*, 847–848.

(23) Noh, M.; Johnson, C. D.; Hornbostel, M. D.; Thiel, J.; Johnson, D. C. *Chem. Mater.* **1996**, *8*, 1625–1635.

(24) Van der Pauw, L. J. *Philips Tech. Rev.* **1958**, 220–224.

(25) Alemayehu, M. B.; Falmbigl, M.; Grosse, C.; Ta, K.; Fischer, S. F.; Johnson, D. C. *J. Alloys Compd.* **2015**, *619*, 861–868.

(26) Phung, T. M.; Jensen, J. M.; Johnson, D. C.; Donovan, J. J.; Mcburnett, B. G. *X-Ray Spectrom.* **2008**, *37*, 608–614.

(27) John J. Donovan; Tracy N. Tingle. *Microsc. Soc. Am.* **1996**, *2*, 1–7.

(28) Heideman, C.; Nyugen, N.; Hanni, J.; Lin, Q.; Duncombe, S.; Johnson, D. C.; Zschack, P. *J. Solid State Chem.* **2008**, *181*, 1701–1706.

(29) Nellist, P. D.; Pennycook, S. J. *The principles and interpretation of annular dark-field Z-contrast imaging*; 2000; Vol. 113.

(30) Nellist, P. D. *Scanning Transmission Electron Microscopy*; 2011.

(31) Oosawa, Y.; Gotoh, Y.; Akimoto, J.; Tsunoda, T.; Sohma, M.; Onoda, M. *Jpn. J. Appl. Phys.* **1992**, *31*, 1096–1099.

(32) Kershaw, R., Vlasse M., W. A. **1967**, *6*, 1965–1968.

(33) Beekman, M.; Disch, S.; Rouvimov, S.; Kasinathan, D.; Koepernik, K.; Rosner, H.; Zschack, P.; Neumann, W. S.; Johnson, D. C. *Angew. Chemie - Int. Ed.* **2013**, *52*, 13211–13214.

(34) Meerschaut, A.; Deudon, C. *Mater. Res. Bull.* **2001**, *36*, 1721–1727.

(35) Krebs, H.; Lagner, D. *Zeitschrift für Anorg. und Allg. Chemie* **1964**, *334*, 37–49.

(36) Alemayehu, M. B.; Falmbigl, M.; Ta, K.; Johnson, D. C. *Chem. Mater.* **2015**, *1*.

(37) Lee, H. N. S.; McKinzie, H.; Tannhauser, D.S.; Wold, A. *J. Appl. Phys.* **1969**, *40*, 602.

(38) Sumesh, C. K.; Patel, M.; Patel, K. D.; Solanki, G. K.; Pathak, V. M.; Srivastav, R. *Eur. Phys. J. Appl. Phys.* **2011**, *53*, 10302.

(39) Madelung, O.; Rossler, U.; Schulz, M. *Tin selenide (SnSe) transport properties*; 1998.